

A Simulation Approach Including Underresolved Scales for Two-Component Fluid Flows in Multiscale Porous Structures

Hiroshi Otomo*, Rafael Salazar-Tio, Jingjing Yang, Hongli Fan, Andrew Fager, Bernd Crouse, Raoyang Zhang and Hudong Chen

Dassault Systèmes, 185 Wyman Street, Waltham, MA 02451, USA.

Received 2 February 2022; Accepted (in revised version) 14 August 2022

Abstract. In this study, we develop computational models and a methodology for accurate multicomponent flow simulation in underresolved multiscale porous structures [1]. It is generally impractical to fully resolve the flow in porous structures with large length-scale differences due to the tremendously high computational expense. The flow contributions from underresolved scales should be taken into account with proper physics modeling and simulation processes. Using precomputed physical properties such as the absolute permeability, K_0 , the capillary pressure-saturation curve, and the relative permeability, K_r , in typical resolved porous structures, the local fluid force is determined and applied to simulations in the underresolved regions, which are represented by porous media. In this way, accurate flow simulations in multiscale porous structures become feasible.

To evaluate the accuracy and robustness of this method, a set of benchmark test cases are simulated for both single-component and two-component flows in artificially constructed multiscale porous structures. Using comparisons with analytic solutions and results with much finer resolution resolving the porous structures, the simulated results are examined. Indeed, in all cases, the results successfully show high accuracy with proper input of K_0 , capillary pressure, and K_r . Specifically, imbibition patterns, entry pressure, residual component patterns, and absolute/relative permeability are accurately captured with this approach.

AMS subject classifications: 52B10, 65D18, 68U05, 68U07

Key words: Multiscale simulation, porous media, multicomponent flow, lattice Boltzmann method.

1 Introduction

The numerical simulation of multicomponent fluid flows in porous regions with complex solid structures is of great importance in many industrial applications such as enhanced

*Corresponding author. *Email address:* Hiroshi.Otomo@3ds.com (H. Otomo)

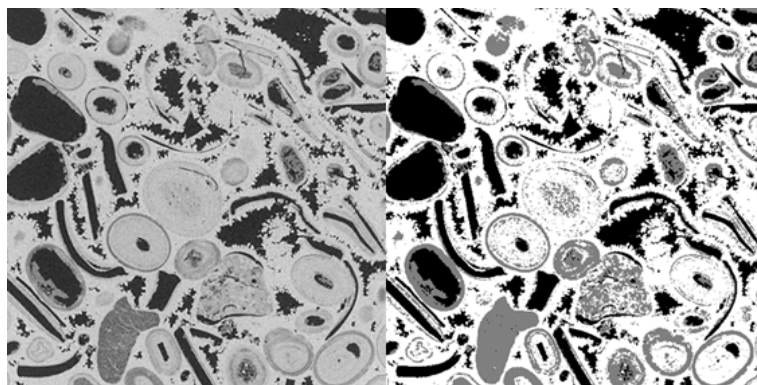


Figure 1: Cross-section pictures of a carbonate rock. An original scanned picture (left) and a segmented picture with small-scale porous structures marked in gray (right) are shown.

oil recovery including carbon dioxide injection, capture and storage [2,3], water/air flow in gas diffusion layers of fuel cells, [4–6], in situ copper mining by leaching [7], and sophisticated personal protective equipment [8]. To achieve high-fidelity simulation, it is crucial to fully resolve complex solid boundaries. In most simulation cases, however, fully resolving all details of a multiscale porous structure is infeasible due to limited machine power and the immaturity of computational models and algorithms, although such complex structures are frequently observed in nature.

Here is an example from an oil&gas industry application. Fig. 1 shows a typical cross-section of a carbonate rock sample that has porous structures with multiple different scales [9]. The left picture shows one slice of an original microtomography scanned image, and the right picture shows its segmented image with small-scale porous structures marked in gray. The length-scale difference between black and gray structures is approximately tenfold. The small-scale porous regions in gray could significantly impact the flow behavior on a large scale because they can contribute to the connectivity among larger-scale pores and can lead to high capillary forces and variable flow resistivity. Therefore, it is necessary to properly consider their contributions. However, resolving all such small-scale details requires extremely fine resolutions, which results in a tremendously expensive simulation. The cost could increase by a factor of tens of thousands compared to the unresolved case, ignoring the contributions of small porous structures from the gray regions because of the increased number of three-dimensional cells and the reduction of time increments. Therefore, such fully resolved simulations are impractical in industrial applications.

In many previous studies [10–16], the viscous force from underresolved porous media (PM) was modeled by a resistance term, as in the Brinkman equation, using a precomputed permeability in the resolved PM with finer resolutions. These studies, however, mainly focused on single-component fluid flow and did not extend to multicomponent fluid flow. A few recent studies [17, 18] have discussed multicomponent fluid flow in multiscale porous structures. In reference [17], the relative permeability from underre-

solved PM regions was computed by solving the transport equation for the total energy, Helmholtz free energy and kinetic energy, without referring to physical properties such as the capillary pressure curves. In reference [18], the precomputed capillary pressure and the effective flow resistance in the resolved PM were applied to derive a force balance analysis at the capillary equilibrium state using recursive methods. Due to the sensitivity of multicomponent fluid flow to the initial flow conditions, it is desirable to solve the unsteady fluid dynamics equation, even when capturing the steady state. In this study, we solve equations based on unsteady fluid dynamics following conditions in laboratory experiments. In addition to improving accuracy, this approach allows us to check the transition of component distributions and flow patterns. Moreover, processing both the input and output data for the PM model using a single solver can contribute to simulation robustness in a significant way.

Here, we propose a solution based on the lattice Boltzmann method, although the methodology itself is not limited to it. In the proposed workflow, computational models are implemented to consider the effects of fluid flow in the underresolved regions. This approach should be applicable for various engineering cases of multiscale porous systems whose length scales typically range from micrometers to millimeters as long as the flows are well within the continuous, Stokes and capillary flow regimes. For example, hydrocarbon reservoir rocks, which are natural porous media, could contain not only intergranular pores but also microporous minerals such as clays [2, 3, 7]. For battery fuel cells and electrolyzers in renewable energy applications, it is typical to encounter microporous electrodes separated by nanoporous membranes [4–6]. In composite applications, fibers can be arranged in bundles to form textile-like large-scale structures as well as extremely small-scale microstructures between individual fibers [8].

This paper is organized as follows. A basic formalism of the lattice Boltzmann method (LBM) for multicomponent fluid flow is introduced in Section 2. The proposed workflow and numerical models for treating multiscale structures are presented in Section 3. In Section 4, detailed settings and results in a set of benchmark test cases for single-component and two-component fluid flows are shown. Finally, in Section 5, the findings of this study are summarized.

2 Lattice Boltzmann models for immiscible fluids

Lattice Boltzmann models for immiscible fluids based on the Shan-Chen model [20, 21] and its recent advancements [19, 22–25] are introduced in this section. The lattice Boltzmann (LB) equation for multicomponent fluids is:

$$f_i^\alpha(\vec{x} + \vec{c}_i \Delta t, t + \Delta t) - f_i^\alpha(\vec{x}, t) = C_i^\alpha + \mathcal{F}_i^\alpha, \quad (2.1)$$

for space \vec{x} and time t , where f_i^α is the density distribution function of fluid component α and \vec{c}_i is the discrete particle velocity. In this study, a binary mixture of immiscible fluids, such as water and oil, is considered for simplicity, namely, $\alpha = \{water(w), oil(o)\}$,

although the framework can be easily extended to an arbitrary number of components. The D3Q19 [26] lattice model with fourth-order lattice isotropy is employed.

The simplest form of the collision operator C_i^α is the Bhatnagar-Gross-Krook type,

$$C_i^\alpha = -\frac{1}{\tau_{mix}}(f_i^\alpha - f_i^{eq,\alpha}), \quad (2.2)$$

where $f_i^{eq,\alpha}$ is the equilibrium distribution function for the Stokes flow with the third order expansion in \vec{u} ,

$$f_i^{eq,\alpha} = \rho_\alpha w_i \left[1 + \frac{\vec{c}_i \cdot \vec{u}}{T_0} + \frac{(\vec{c}_i \cdot \vec{u})^3}{6T_0^3} - \frac{\vec{c}_i \cdot \vec{u}}{2T_0^2} \vec{u}^2 \right], \quad (2.3)$$

where $T_0 = 1/3$ and w_i denote the lattice temperature and isotropic weights in D3Q19, respectively. The density of the components α and ρ_α and the mixture flow velocity, \vec{u} , are defined as

$$\rho_\alpha = \sum_i f_i^\alpha, \quad \rho = \sum_\alpha \rho_\alpha = \sum_\alpha \sum_i f_i^\alpha, \quad \vec{u}^\alpha = \sum_i \vec{c}_i \cdot f_i^\alpha / \rho_\alpha, \quad \vec{u} = \sum_\alpha \sum_i \vec{c}_i \cdot f_i^\alpha / \rho. \quad (2.4)$$

The relaxation time τ_{mix} in Eq. (2.2) relates to the kinematic viscosity of the mixture of components, ν_{mix} , as

$$\tau_{mix} = (\nu_{mix} / T_0) + 1/2, \quad (2.5)$$

$$\nu_{mix} = (\rho_w \nu_w + \rho_o \nu_o) / (\rho_w + \rho_o). \quad (2.6)$$

According to Ref. [19], the forcing term \mathcal{F}_i^α in Eq. (2.1) is formulated involving the inter-component force, $\vec{F}^{\alpha,\beta}$, between components α and β ,

$$\vec{F}^{\alpha,\beta}(\vec{x}) = G \rho_\alpha(\vec{x}) \sum_i w_i \vec{c}_i \rho_\beta(\vec{x} + \vec{c}_i \Delta t), \quad (2.7)$$

for $\alpha \neq \beta$, and $\vec{F}^{\alpha,\beta}(\vec{x}) = 0$ for $\alpha = \beta$ following the conventional way [20,21]. When the interaction strength G is negative, a repulsive force acts between components and yields a phase separation. In this paper, G is chosen so that the surface tension σ is 0.025. The acceleration of the component α , \vec{g}_α , originating from $\vec{F}^{\alpha,\beta}$ is defined as $\vec{g}_\alpha = \sum_\beta \vec{F}^{\alpha,\beta} / \rho_\alpha$. The resulting fluid velocity \vec{u}_F is defined as the averaged velocity over pre- and postcollision steps and written as

$$\vec{u}_F = \vec{u} + \vec{g} \Delta t / 2, \quad \vec{g} = \sum_\alpha \vec{g}_\alpha \rho_\alpha / \rho. \quad (2.8)$$

In what follows, this quantity \vec{u}_F is called *velocity*.

To enhance stability and accuracy when τ_{mix} is not close to 1, a regularized collision operator is used. Rearranging Eq. (2.1), one obtains

$$f_i^\alpha(\vec{x} + \vec{c}_i \Delta t, t + \Delta t) = f_i^{eq,\alpha} + \left(1 - \frac{1}{\tau_{mix}}\right) f_i'^\alpha + \mathcal{F}_i^\alpha, \quad (2.9)$$

where the function $f_i^{\prime\alpha}$ is the nonequilibrium particle distribution for each fluid component. If $f_i^{\prime\alpha}$ takes the standard BGK form, $f_i^\alpha - f_i^{eq,\alpha}$, and τ_{mix} is away from 1, one suffers from the instability caused by numerical artifacts from the LB model. To address this issue, a collision procedure regarding $f_i^{\prime\alpha}$ is regulated as

$$f_i^{\prime\alpha} = \Phi^\alpha : \Pi^\alpha. \quad (2.10)$$

Here, Φ is a regularization operator that uses Hermite polynomials, and Π^α is the nonequilibrium part of the momentum flux. The basic concept of the regularized collision procedure can be found in [22–25, 27–29].

For accurate no-slip wall boundary conditions on arbitrary geometries, an extension of the volumetric boundary condition proposed by Chen et al. in 1998 [30–33] is employed. In this method, after boundary surfaces are discretized into linear surface facets in two dimensions or triangular polygons in three dimensions, the incoming and outgoing particles based on those facets or polygons are computed in a volumetric way obeying the conservation laws. This method is generalized for BCs on arbitrary geometry, and it has been studied extensively. More details can be found in [30]. To mitigate numerical smearing in the near-surface region, especially when the physical viscosity is small and the resolution is coarse, the surface scattering model presented in [31] is useful.

For the surface wetting conditions, the intercomponent interaction force in Eq. (2.7) is extended to the interaction force between the wall and fluid particles, $\vec{F}_w^{\alpha,\beta}$, as

$$\vec{F}_w^{\alpha,\beta}(\vec{x}) = G\rho_\alpha(\vec{x}) \sum_i w_i \vec{c}_i \rho_\beta'(\vec{x} + \vec{c}_i \Delta t), \quad (2.11)$$

for $\alpha \neq \beta$, and $\vec{F}_w^{\alpha,\beta}(\vec{x}) = 0$ for $\alpha = \beta$, where ρ_β' is constructed of a fluid part and a solid part ρ_β^s in a volumetric way so that $\partial\rho_\beta/\partial n$ is close to zero [30]. This volumetric wettability scheme has a sufficient isotropy on complex geometries [34–36]. The wall potential for components ρ_w^s and ρ_o^s is defined as

$$\rho_w^s = -\rho_0 \rho^s \Theta(-\rho^s), \quad \rho_o^s = \rho_0 \rho^s \Theta(\rho^s), \quad (2.12)$$

using a single parameter ρ^s , where Θ is the Heaviside function and ρ_0 is 1.0.

3 Numerical models and workflow for multiscale porous structures

In a multiscale fluid-flow simulation at a certain resolution level, flow contributions from underresolved porous regions are properly considered by applying numerical models at each site using local information of the geometry and fluids. The models reproduce proper forces acting on fluids, such as viscous, pressure, and capillary forces, using local representative physical properties, such as absolute permeability K_0 , relative permeability K_r^α and capillary pressure-saturation curves $P_C - S_w$, where α is an index for the

fluid component. As a first step, CT scanned images of the porous geometry are analyzed. Small-scale porous structures, which are underresolved in the flow simulation, are characterized into a few porous types with assigned type IDs such that the underresolved porous structures can be effectively represented by those porous types. Next, the physical properties for each porous type are precomputed using a fine resolution to fully resolve the porous structure in the representative tiny subdomain of the original porous structure. Once finished, the results are registered and stored in a library. Each set of physical properties mentioned above represents a flow type for the particular underresolved porous structure type. Last, for a multiscale simulation with a practical resolution, referring to the type ID assigned in each underresolved region, one selects a set of physical properties of the porous type from the library and uses it for computing the local forces acting on the fluid. To properly consider the detailed local structures, the local porous geometry information sources, including porosity ϕ (the ratio of fluid volume to total volume) and directionality of the structure, are also utilized to formulate the force.

The workflow is further illustrated in Fig. 2. The left top scanned image is an image coarsened from a high-resolution scanned image that resolves all porous structures of interest. This image indicates a multiscale flow simulation, with black, gray, and white colors representing pores, underresolved porous structures, and solids, respectively. The multiscale flow simulation is performed with the same resolution as this scanned image. The detailed procedures are as follows.

- i. Conduct a geometrical analysis for the original image and categorize the porous structures [38]. Then, the porous structure in each underresolved region, i.e., the gray region in Fig. 2 is labeled by a porous type ID according to the analysis. Such a categorization allows us to simplify the representation of multiple porous regions using only a few different types. In Fig. 2, four possible types are illustrated. Regions belonging to the same category or type not only look similar but also share similar physical properties, as represented by the curves in Fig. 2.
- ii. Define a flow model for each underresolved region and check existing sets of physical properties corresponding to the typed porous structure in the library. If the corresponding set of physical properties already exists, pick it up from the library. If not, conduct a fully resolved simulation in a representative subdomain using the fully resolving original scanned images, compute the new set of physical properties, including absolute permeability, relative permeability, and capillary pressure-saturation curves for this particular type of porous structure, and add it to the library utilized for the multiscale simulation. Detailed settings in such a simulation are shown in the beginning of Section 4 as an example.
- iii. Construct and apply fluid force at each underresolved site using the constitutive relationships according to the local geometry information and physical properties. This

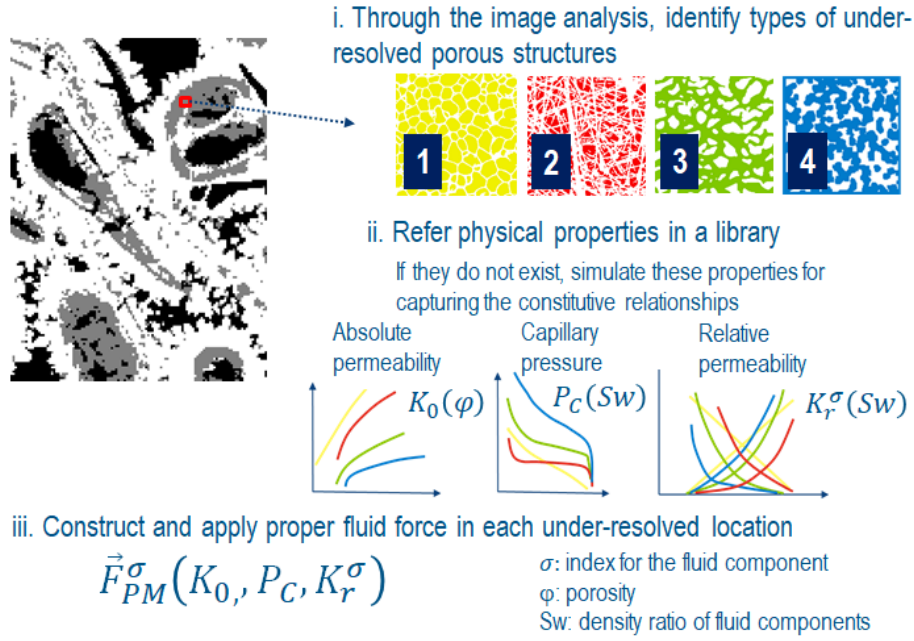


Figure 2: Steps for a multiscale simulation.

force corresponds to viscous, pressure and capillary forces from the underresolved solid structure.

There are various ways to define numerical models for fluid force in underresolved regions. Here, we show one possible example. Under an assumption of a homogeneous solid structure in an underresolved porous region, the viscous force in the underresolved PM region is computed using K_0 and K_r^α as

$$\vec{F}_{PM_{vis}}^\alpha = -\frac{\nu_\alpha}{K_0 K_r^\alpha} \rho_\alpha \vec{u}_F. \quad (3.1)$$

Here, K_0 and K_r^α are the main inputs of the model and functions of porosity ϕ and density ratio of fluid components $S_w = \rho_w / (\rho_w + \rho_o)$.

On the other hand, an example for a definition of capillary force $\vec{F}_{PM_{cap}}^\sigma$ can be written as

$$\vec{F}_{PM_{cap}}^\alpha = -\frac{2\sigma \cos\theta \cdot \mathcal{J}}{\sqrt{K_0 K_r^\alpha} / \phi} \frac{\hat{\nabla} \rho_o - \hat{\nabla} \rho_w}{2} \cdot H(At, |\partial_x(At)|), \quad (3.2)$$

where the hat notation indicates the unit vector and θ is the contact angle of the underresolved porous solid. Here, \mathcal{J} is the Leverett J-function, defined as $P_c \sqrt{K_0 K_r^\alpha} / \phi / \sigma \cos\theta$, which is the normalized capillary pressure and function of S_w and ϕ . Here, P_c is one of the main inputs of the model and is the function of S_w . The Atwood number, At , is defined

as $At = (\rho_w - \rho_o) / (\rho_w + \rho_o)$. A functional H is a switch function depending on the local multicomponent interface condition. This switch function is necessary for the diffusive multicomponent model because its nonzero interface thickness may cause excessive artificial force. Moreover, this definition cannot cover a scenario where a component fluid is confined in an underresolved cell due to its internal structures. To mitigate this problem, an additional model can be implemented. For example, the drainage and stagnation of residual components in a computational cell under a certain local pressure and S_w is controlled by referring to the Leverett J-function.

The wettability effects originating from solid parts in the PM site can be considered by simply extending Eq. (2.11). Specifically, ρ'_β is constructed by a wall potential from the porous solid, ρ_β^{sPM} , and the fluid density ρ_β with the ratio of ϕ as

$$\rho'_\beta = \phi \rho_\beta + (1 - \phi) \rho_\beta^{sPM}, \quad (3.3)$$

where no adjacent regular solid, the resolvable solid, exists. This natural extension for the PM model is one of motivations to employ the LBM in this study. Additionally, in a computational cell with small porosity, the wettability and friction effects from the regular solid may be suppressed. This is because the confined fluid in the porous media cannot be influenced by the adjacent regular solids, and wettability and friction effects are already considered in the PM region via the inputs K_0 , K_r , and P_C .

4 Validation

The numerical models and workflow introduced in Section 2 and Section 3 are validated through a set of benchmark test cases for single-component and two-component fluid flows. As a representative porous structure underresolved in the multiscale simulation, geometrical data are constructed based on open-source data [9], as shown in Fig. 3. The domain size is $256 \times 256 \times 256$, and the resolution is $1 \mu\text{m} / \text{pixel}$. The global porosity, ϕ_{glb} , is 38%. First, we simulate several cases in this system to obtain inputs for the following multiscale simulations. In the simulation for computing $K_0(\phi)$, the domain is mirrored, and periodic boundaries are assigned in the flow direction. Then, gravity g is assigned as the driving force. The other domain edges are bounded by solid walls. The values of viscosity ν and g are set as $\nu = 0.012$ and 1.0×10^{-4} so that the velocity is in the reasonable range and the Reynolds number is sufficiently small. We evaluate K_0 as $\phi_{glb} < u > \nu / g$, where $< u >$ is the spatially averaged fluid velocity. This K_0 computation is individually performed for the eight-cube domain, which is equally divided from the original domain. In the simulation for computing $P_C(S_w)$, the oil initially fills the entire domain of the original geometry plus the oil reservoir of the top 14 lattice layers. The dominant oil/water pressure boundaries are assigned on the top/bottom ends. Their pressure difference ΔP is initially set as a high value and timely controlled while fixing the pressure in the bottom boundary as 7.33×10^{-2} . Specifically, if the temporal variation of S_w drops below a certain value, a controller judges this as the steady state and shifts ΔP to the next level.



Figure 3: A representative porous structure applied for the underresolved regions in the multiscale simulation in Section 4.

The PM and sidewalls surrounding the PM are assumed to be water-wet with a contact angle of 10 degrees. Viscosities for both fluid components are set to $\nu_w = \nu_o = 1.66 \times 10^{-3}$ so that the capillary number is sufficiently small. In the simulation for computing the relative permeability for water and oil, $K_{rw}(S_w)$ and $K_{ro}(S_w)$, the domain is mirrored, and periodic boundaries are assigned in the flow direction. Gravity g is assigned as the driving force. Initially, in addition to the oil mainly occupying the domain, a small amount of water is distributed in the relatively small-sized pores. A controller program adjusts the gravity so that the target capillary number, $Ca = 1.0 \times 10^{-6}$, is achieved at the steady state. Once the flow reaches the targeted steady state, using a mass-sink-source (MSS) function [39], the water is injected locally with criteria of local At and velocity fields. Once S_w reaches the targeted level, the MSS is switched off, and the controller adjusts the gravity for the next targeted Ca again. This loop is iterated until the relative permeability for all S_w is evaluated. Wettability conditions are set similarly to the P_C simulation. Viscosities for both components are set as $\nu_w = \nu_o = 3.33 \times 10^{-3}$ so that the Reynolds number is sufficiently small.

The simulated $K_0(\phi)$, $P_C(S_w)$, $K_{rw}(S_w)$, and $K_{ro}(S_w)$ are fitted with the Kozney-Carman equation, Thommer model, and Corey model, respectively;

$$K_0(\phi) = \frac{D(\phi - \phi_p)^2}{72\tau_p^2(1 - (\phi - \phi_p))^2}, \quad (4.1)$$

$$P_C(S_w) = P_c^* \cdot \exp\left(\frac{\Delta P_C^*}{\ln(S_w/S_{wref})}\right), \quad (4.2)$$

$$K_{rw}(S_w) = \left(\frac{S_w - S_{wi}}{1 - S_{wi} - S_{or}}\right)^{n_w}, \quad (4.3)$$

$$K_{ro}(S_w) = \left(\frac{1 - S_w - S_{or}}{1 - S_{wi} - S_{or}}\right)^{n_o}. \quad (4.4)$$

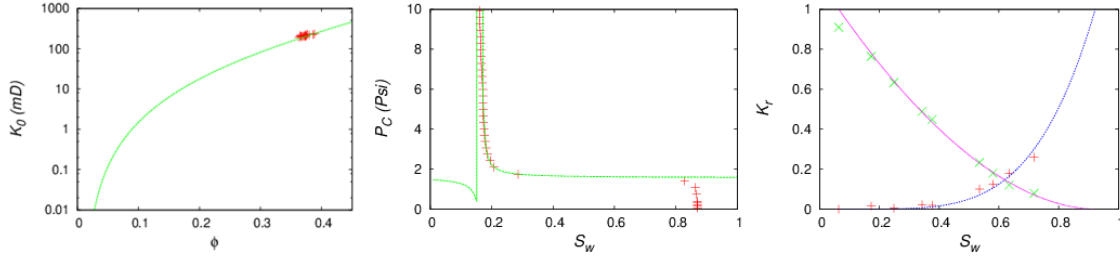


Figure 4: Simulated absolute permeability vs porosity (left), the capillary pressure vs water saturation S_w (center), and the relative permeability vs S_w (right) in the PM of Fig. 3. Their fitted results are plotted with lines.

The results for the simulation points and fitting curves are shown below and Fig. 4;

$$\begin{aligned}
 D &= 801800 [\text{mD}], \quad \tau_p = 2.5, \quad \phi_p = 0.01, \\
 P_c^* &= 1.515 [\text{Psi}], \quad \Delta P_c^* = 0.0831, \quad S_{wref} = 0.161, \\
 S_{wi} &= 0.065, \quad S_{or} = 0.07793, \quad n_w = 4.408, \\
 n_o &= 1.844.
 \end{aligned} \tag{4.5}$$

Henceforth, unless specifically mentioned, they are used as standard inputs for the PM model in the multiscale simulation.

4.1 Force balance check in single-component fluid flow through porous media

The modeled resistance force from the PM in Eq. (3.1) is validated by checking the force balance in single-component fluid flow through a PM region. In an arbitrary small domain bounded by periodic boundaries, the PM model is applied everywhere while gravity g is assigned. The expected force balance can be formulated as $\rho r \cdot (\phi u) = \rho g$, where r is the resistivity from the PM model, $r = \nu / K$, ϕ is the porosity, and u is the fluid velocity. Various options of viscosity ν , g , and r are tested. Here, r is controlled by setting the input K as certain constant numbers. Table 1 shows the resulting $r \cdot (\phi u)$. They agree with input g very well. Remembering the definition of $K_0 = \phi u \nu / g$, we see that this force balance also indicates the consistency between input K_0 , $K_{0,in}$ and output K_0 , $K_{0,out}$. This is because $K_{0,in} = \nu / r = \phi u \nu / g = K_{0,out}$, where the formulation of r is used in the first equation and the force balance is used in the second equation.

Table 1: Results of force balance check in the gravity driving flow through PM.

ν	r	g	$r \cdot (\phi u)$
1.67×10^{-3}	8.32×10^{-3}	5.00×10^{-4}	5.00×10^{-4}
3.33×10^{-2}	1.66×10^{-1}	1.00×10^{-2}	1.00×10^{-2}
1.67×10^{-1}	8.32×10^{-1}	5.00×10^{-2}	5.00×10^{-2}

4.2 Single-component fluid flow through multitype porous media

Two-dimensional single-component fluid flow through spatially varied porous structures is simulated. In a simulation domain of 200×100 , circular-shaped porous medium PM2, whose diameter is 40, is surrounded by the other typed porous medium PM1, as shown in Fig. 5. Many options of the input permeability for PM2 are tried from 1 mD to 5000 mD, while one for PM1 is fixed at 100 mD. The resolution is assumed to be $31.25 \mu\text{m}/\text{pixel}$. Gravity is assigned in the horizontal direction, and its value is low enough to realize the Stokes flow regime. The viscosity ν is set as 1.66×10^{-3} .

The simulated permeability, $K_{0,sim} = \phi_{glb} \langle u \rangle / g$, where ϕ_{glb} is the global porosity, is presented in Table 2 together with the Darcy solver's results. In the Darcy solver, the force balance between the driving and resistance terms in the Brinkman equation is solved at each definition point [37]. Since it ignores the viscous terms and temporal derivative terms, it is applicable only for limited cases in the multiscale simulation. In the present case where the entire domain is covered by porous media, however, the Darcy solver outputs consistent results with the present solver within 0.1% deviation. The pressure profiles are compared in Fig. 6 for the case of $K_0 = 1\text{mD}$ in PM2. The pressure value is normalized by $F \cdot L_d$, where F is the driving force and L_d is the domain length. Its absolute value is shifted to zero on the right boundary. Their excellent agreement indicates that

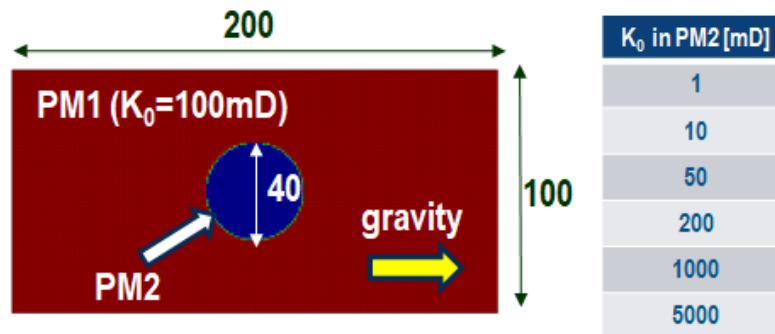


Figure 5: Setups of the single-component fluid flow simulation through various types of porous media.

Table 2: Simulated K_0 through two-dimensional porous structures using the present and Darcy solver.

K_0 in PM2 [mD]	$K_{0,sim}$ (Darcy solver)	$K_{0,sim}$ (Present)	Deviation
1	87.52	87.45	0.08 %
10	89.66	89.61	0.06 %
50	95.83	95.8	0.03 %
200	104.2	104.2	< 0.01 %
1000	110.5	110.4	0.09 %
5000	112.5	112.4	0.09 %

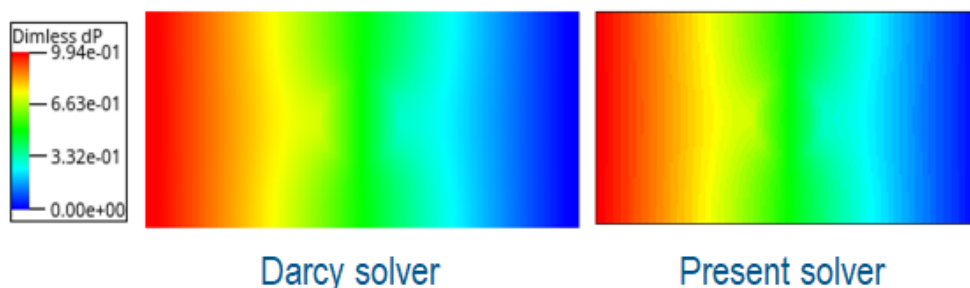


Figure 6: Contours of the pressure profile with the Darcy solver (left) and the present solver (right) in the case of $K_0 = 1mD$ in PM2. The pressure value is normalized by $F \cdot L_d$, where F is the driving force and L_d is the domain length.

the present PM model based on the LBM correctly handles the fluid force of a single component in porous media.

4.3 An imbibition process in one-dimensional porous media

The modeled capillary force from the PM in Eq. (3.2) is examined by checking the force balance between the pressure force and capillary force in the one-dimensional PM region and a pore region. In a simulation domain of 150 lattices, the left half is set as a pore region, and the right half is set as a PM region of $\phi = 0.3$, as shown in Fig. 7. In the PM region, in addition to the standard inputs of $K_0(\phi)$, $K_{rw}(S_w)$, and $K_{ro}(S_w)$ precomputed in Fig. 4, the input function $P_C(S_w)$ is set as the constant value of $P_C = 0.05$. The resolution is assumed to be $4.0\mu m / pixel$. The wettability in the PM region is set as water-wet with a contact angle of 10 degrees. On the right end, the pressure value is set as 0.0733 with $S_w = 0.9995$. On the left end, with $S_w = 0.05$, the pressure value is set so that the pressure difference between both ends, ΔP , is equivalent to 110% or 90% of the assigned P_C in the PM. Initially, oil is mainly filled over the entire domain. The viscosities for both components are $\nu_w = \nu_o = 1.66 \times 10^{-3}$ so that the capillary number is sufficiently low while the velocity magnitude is in the reasonable range.

Snapshots of the water distribution at certain timesteps are shown in Fig. 8. In the top and bottom three figures, the results in cases with $\Delta P = 0.9P_C$ and $\Delta P = 1.1P_C$ are shown, respectively. They indicate that the imbibition process can be accurately simulated within the 10% range of the assigned P_C in the PM.



Figure 7: Settings in a one-dimensional PM case. The red and blue colors show the pore region and PM region of $\phi = 0.3$, respectively. At both the right and left ends, pressure boundaries are imposed.

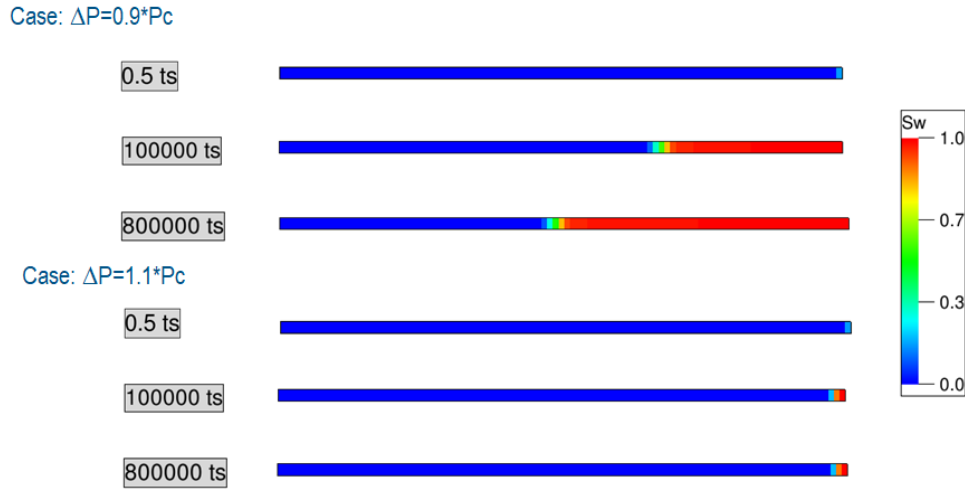


Figure 8: Snapshots of the water distribution at certain timesteps in one-dimensional imbibition processes with the PM model. The top three figures show the case with a pressure difference of 90% assigned P_C in the PM. The bottom three figures show the case with a pressure difference of 110% assigned P_C in the PM.

4.4 An imbibition process in two-dimensional layered channels

A typical sequential imbibition process into pores and PM is examined in two-dimensional layered channels, as shown in the left figure of Fig. 9. In the domain of 44×26 , the center region, colored red, is a pore and regarded as the main channel. On both sides of the main channel, there are two different types of underresolved PMs of $\phi = 0.3$, colored blue and gray. The left/right PM is oil/water-wet with a contact angle of 170/10 degrees. On the top and bottom edges, they are bounded by oil- and water-wet walls of the same contact angles as the adjacent PM regions. The resolution is assumed to be $31.25 \mu\text{m}/\text{pixel}$.

The imbibition process is started with a sufficiently high pressure difference between the inlet and outlet, ΔP . As time goes, ΔP is gradually reduced, as shown in the right figure of Fig. 9. Due to the scale difference between pores and PM, imbibition into the water-wet PM typically occurs at first once ΔP becomes sufficiently low. When ΔP is decreased further and becomes comparable with the capillary pressure in the water-wet pores, the water invades such pores. Later, as ΔP is decreased, in contrast to the water-wet scenario, the water invades the oil-wet pore at first and the oil-wet PM lastly. One of the main motivations in this section is to capture this sequential process quantitatively.

In addition to the standard inputs of $K_0(\phi)$, $K_{rw}(S_w)$, and $K_{ro}(S_w)$ precomputed in Fig. 4 for the PM region, the input function of $P_C(S_w)$ is set as the constant value of $P_{C(wet,PM)} = 0.02$ for the water-wet PM and $P_{C(owet,PM)} = -0.02$ for the oil-wet PM. The pressure value on the right boundary is set as 0.0733 with $S_w = 0.9995$. According to the Laplace law, the capillary pressure in the main channel is expected to be $P_{C(wet,pore)} = \sigma \cos(10^\circ)/h = 4.92 \times 10^{-3}$ for the water-wet pore and $P_{C(owet,pore)} = \sigma \cos(170^\circ)/h =$

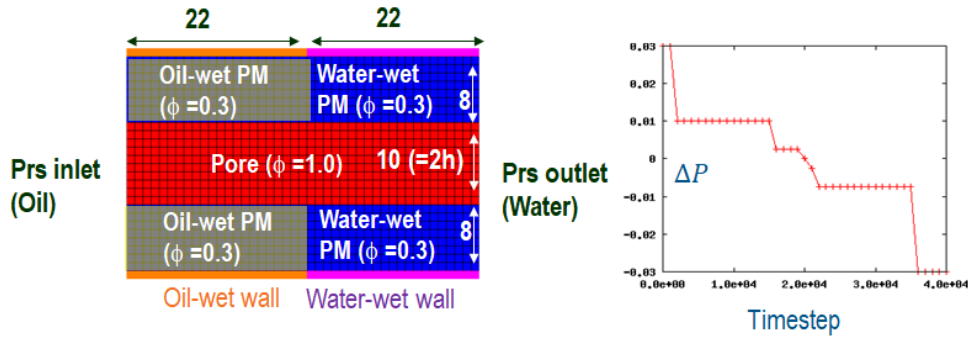


Figure 9: Settings in two-dimensional layered channels (left) and time history of the pressure difference between the left and right ends (right). In the left figure, the red, blue, and gray colors show a pore region, water-wet and oil-wet porous medium of $\phi=0.3$, respectively.

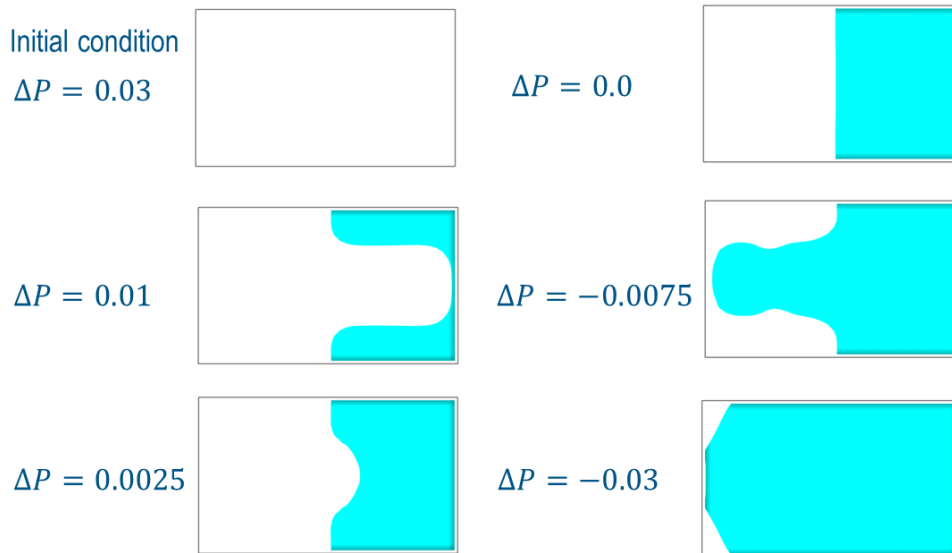


Figure 10: Water isosurface of $At > 0.5$ at six ΔP conditions in two-dimensional layered channels.

-4.92×10^{-3} for the oil-wet pore, where $h = 5$ is the half channel height and $\sigma = 0.025$ is the surface tension. Considering the estimated capillary pressure above, we gradually decrease ΔP from 0.03 to -0.03 by changing the pressure value on the left boundary while fixing $S_w = 0.05$. Initially, oil mainly occupies the entire domain. Viscosities for both components are set as $\nu_w = \nu_o = 1.66 \times 10^{-3}$.

The simulated results are shown in Fig. 10. The water distributions at six ΔP conditions are shown with the isosurface of $At > 0.5$. At $\Delta P = 0.01$, which is below $P_{C(wwet,PM)}$ and above $P_{C(wwet,pore)}$, water invades the water-wet PM. When $\Delta P = 0.0025$ and $\Delta P = 0.0$, which are below $P_{C(wwet,pore)}$ and above $P_{C(owet,pore)}$, water invades the water-wet pore.

When $\Delta P = -0.0075$, which are below $P_{C(owet,pore)}$ and above $P_{C(owet,PM)}$, water invades the oil-wet pore. Last, when $\Delta P = -0.03$, which is below $P_{C(owet,PM)}$, most of the entire domain is filled with water. As a result, the current PM model successfully reproduces the expected sequential imbibition process to pores and PM quantitatively.

4.5 Porous media of a large cone-shaped hole

Using an in-house designed porous structure that has a large cone-shaped hole partially bounded by the solid walls and connects to the PM regions, single-component and two-component fluid flows are simulated using two different resolutions. The PM structures are constructed based on the geometry in Fig. 3. A finer resolution, $1 \mu\text{m}/\text{pixel}$, allows us to resolve all of the PM structures and capture the geometry shown in the left figure of Fig. 11. On the other hand, the coarse resolution, $4 \mu\text{m}/\text{pixel}$, underresolves the PM structures but can resolve only large-scale solid walls on the boundaries between the hole and PM, as shown in the middle figure of Fig. 11.

The PM model in Section 3 is applied only for the underresolved regions in the coarse resolution case, using the porosity distribution presented in the right figure of Fig. 11. The contributions of the resolved and underresolved regions to the global porosity are 41% and 55%, respectively. In this section, we mainly examine the consistency between the fully resolved PM case with fine resolution and the underresolved PM case with coarse resolution. The standard inputs of $K_0(\phi)$, $K_{rw}(S_w)$, and $K_{ro}(S_w)$ precomputed in Fig. 4 are used for the PM model in the underresolved PM case. The resolution of the scanned images is equivalent to the resolution in the flow simulation.

In the simulation for computing K_0 , the domain and gravity are set in the same manner as the K_0 simulation for the PM model in Fig. 3. The domain sizes in the resolved PM case and the underresolved PM case, before mirroring, are $256 \times 256 \times 512$ and

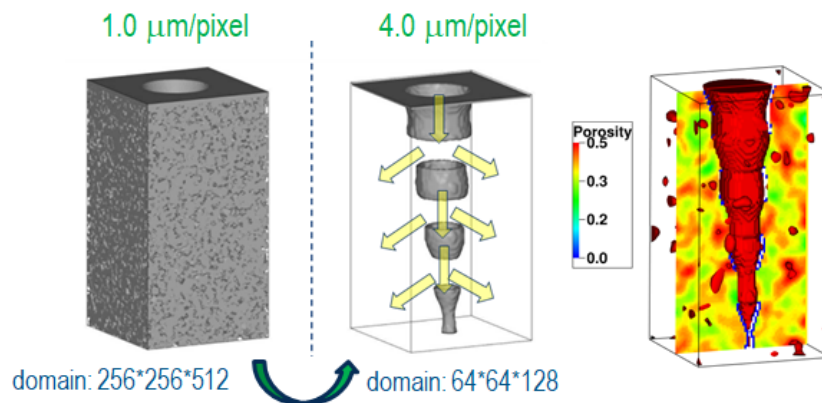
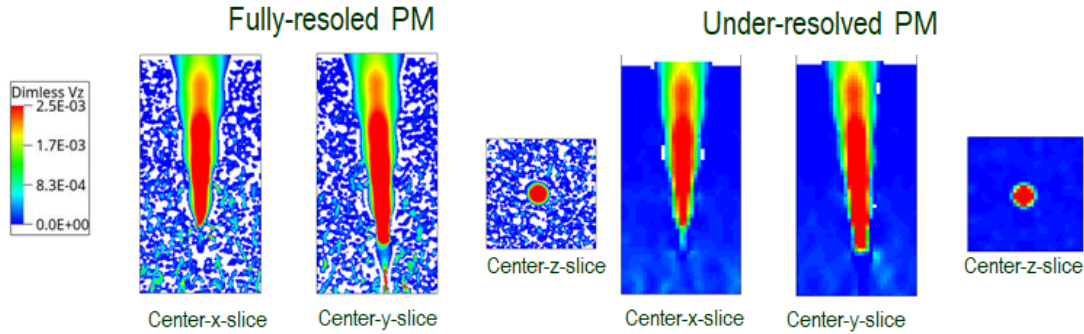


Figure 11: Visualization of porous structures. Solid surfaces in the resolved PM case (left) and in the underresolved PM case (center). The isosurfaces of porosities larger than 0.9 are displayed on the right together with the color contour of the porosity on a center plane.

Table 3: Absolute permeability K_0 in porous media of a large cone-shaped hole.

Case	K_0 (mD)
Fully-resolved PM	458
Under-resolved PM	486

Figure 12: Contour plots of the nondimensional z-velocity using gL^2/ν , where g is gravity, ν is the kinematic viscosity, and L is the characteristic length.

$64 \times 64 \times 128$, respectively. The viscosity is set as $\nu = 0.166$ for the resolved PM case and $\nu = 0.0166$ for the underresolved PM case. The gravity, g , is set as 1.0×10^{-4} for the resolved PM case and 1.5×10^{-4} for the underresolved PM case. They are set so that the mean velocity is almost on the same order of magnitude. Table 3 shows the computed K_0 in the resolved PM and underresolved PM cases. Although the resolved PM case requires more than 20 CPU hours compared to the underresolved PM case, their K_0 values are consistent within 6.1% deviation. The deviation possibly comes from connectivity among the PM cells and improper assignments of input K_0 for the PM model on boundaries between the hole and the PM region. On such boundaries, the homogenous PM models shown in Fig. 3 may not be accurate. Fig. 12 shows comparisons of flow fields on XY-/XZ-/YZ-planes, displayed with the nondimensionalized z-velocity by gL^2/ν , where L is the characteristic length. This shows that the PM model enables us to capture a reasonable flow field even inside the PM. According to our original method in which the underresolved regions are regarded as solid, there are no main flow passages through the domain, and therefore, K_0 results in almost zero. The proposed methods and the PM model address this issue effectively and provide accurate K_0 and velocity profiles while largely saving computational costs

In the simulation for computing P_C , the domain settings, initial conditions, and simulation processes follow the same manner as the P_C simulation for the PM in Fig. 3. Viscosities for both components are set as $\nu_w = \nu_o = 1.66 \times 10^{-3}$. The resulting capillary pressure, ΔP , in terms of the water saturation S_w is shown in the left figure of Fig. 13. Here, a

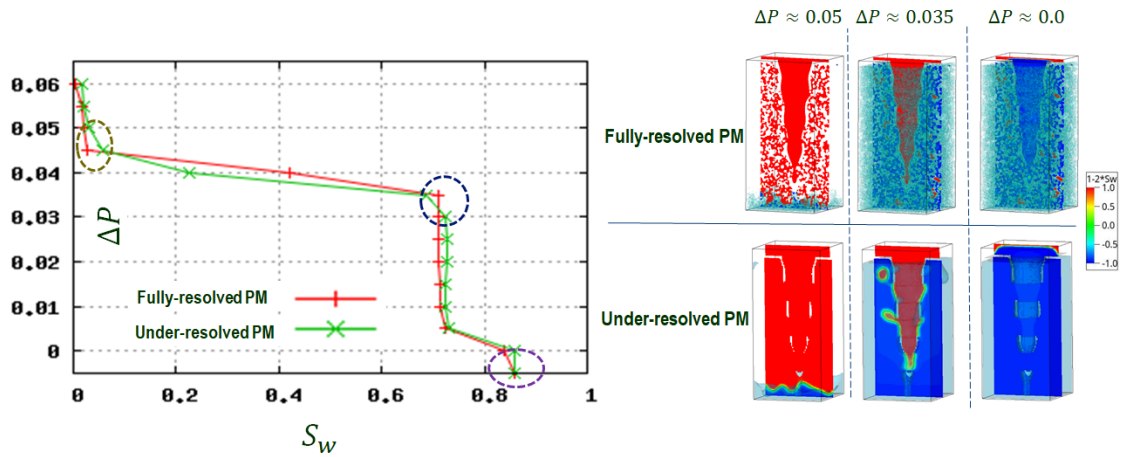


Figure 13: Capillary pressure curve in terms of water saturation S_w in the resolved PM case and the underresolved PM case in the left figure. In the right figures, the water distributions at certain stages, marked with dotted circles in the left figure, are shown for both cases using the isosurface of $At > 0.5$ and color contour of At on the central cutting plane.

resolution factor 4 is multiplied by ΔP of the resolved PM case for fair comparisons in the lattice unit. The water distributions at certain stages, marked with the dotted circles in the left figures, are shown in the right figures using the light-blue isosurfaces of $At > 0.5$ and color contours on the central cutting plane. The capillary pressure curves show that the main entry pressure around $\Delta P = 0.045$ is accurately captured with the PM model compared to the resolved PM case within 5% deviation. This main entry occurs in the PM region, and therefore, the accuracy of the input P_C curve plays an important role. Additionally, the entry pressure into the large hole around $\Delta P = 0.005$ is accurately captured with the PM model. As seen in the right figures of Fig. 13, some oil bubbles are observed in the PM region in the middle of imbibition. They are possibly caused by the difficulty in capturing the exact steady state. This is because the dynamics in the PM region are usually very slow due to the high viscous force from the complex porous structure and complex invasion paths. As a result, the simulation controller sometimes insufficiently judges the steady state and proceeds to the next stage. Nevertheless, the capillary pressure curves in the underresolved PM and resolved PM cases are reasonably matched, while the simulation time is reduced by a factor of 30.

4.6 Porous media made from a typical carbonate rock

Using an in-house designed PM geometry made from images of a typical carbonate rock [9], single-component and two-component fluid flows are simulated using two different resolutions. To explicitly produce multiscale structures, the porous structures in Fig. 3 are patched to the original images as small-scale PM structures. Specifically, the images of Fig. 3 are patched while scaling them so that a resolution of $0.758 \mu\text{m}/\text{pixel}$ allows us to resolve all PM structures. As a result, the geometry shown in the left figure of

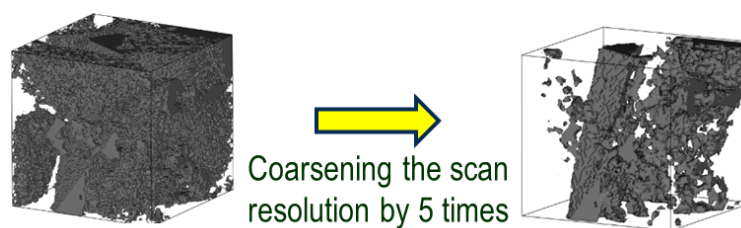


Figure 14: PM structures captured with a resolution of $0.758 \mu\text{m}/\text{pixel}$ (left) and a resolution of $3.79 \mu\text{m}/\text{pixel}$.

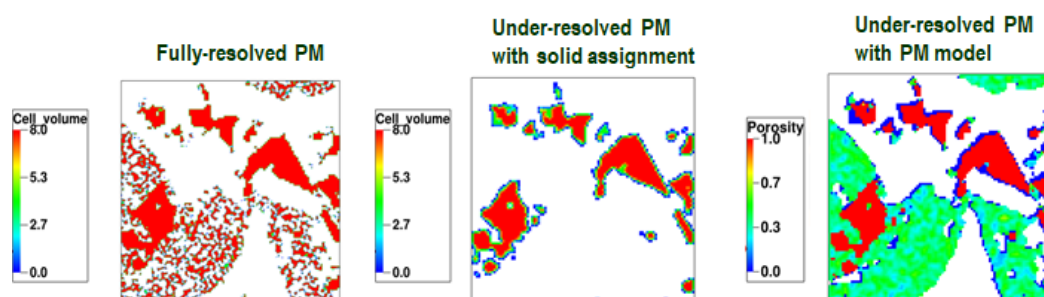


Figure 15: Geometries of simulated fluid cells under three different conditions. The fluid cells in the resolved PM case with the color contours of the cell volume (left). The fluid cells captured with the coarse resolution where the underresolved PM is regarded as the solid (middle). The fluid cells captured with the coarse resolution plus fluid cells handled by the PM model together with the colored porosity distribution.

Fig. 14 is captured at this resolution. Then, the images are coarsened 5 times. The coarse resolution, $3.79 \mu\text{m}/\text{pixel}$, underresolves small-scale PM but can resolve only large-scale PM structures shown in the right figure of Fig. 14. The resolution of the scanned images is equivalent to the resolution in the flow simulation. The contributions of the resolved and underresolved regions to the global porosity are 27% and 19%, respectively. Originally, the underresolved PM regions were treated as solid in the simulation, but now they can be handled by the PM model. In the sense of clarification, geometries of fluid cells on a certain cross section are presented for three compared conditions in Fig. 15. The left figure shows the fluid cells in the resolved PM case of the fine resolution with color contours of fluid volume. The middle figure shows the fluid cells captured with the coarse resolution, where the underresolved PM is regarded as solid. This indicates that many small-scale structures are missed compared to the resolved PM case. The right figure shows that the fluid cells captured with the coarse resolution plus the fluid cells handled by the PM model using the colored porosity distribution. It explicitly shows that the connectivity among large-scale PMs is enhanced compared to the middle figure. For the PM settings, the standard input of $K_0(\phi)$, $P_C(S_w)$, $K_{rw}(S_w)$ and $K_{ro}(S_w)$ precomputed in Fig. 4 are used.

In the simulation for computing K_0 , the domain and gravity are set in the same manner as the K_0 simulation in Fig. 4. The domain sizes in the resolved PM case and the

Table 4: Absolute permeability K_0 in the PM made from a typical carbonate rock.

Case	K_0 (mD)
Resolved PM	2121
Underresolved PM with the solid assignment	2040
Underresolved PM with the PM model	2279

underresolved PM case are $500 \times 500 \times 500$ and $100 \times 100 \times 100$, respectively. The viscosity is set as $\nu = 0.166$ for the resolved PM case, $\nu = 0.0166$ for the underresolved PM case with the solid-wall assignment, and $\nu = 0.012$ for the underresolved PM case with the PM model. The gravity, g , is set as 5.7×10^{-6} for the resolved PM case and 1.4×10^{-3} and 1.4×10^{-5} for the two underresolved PM cases. They are determined so that the mean velocity is approximately on the same order of magnitude while the Reynolds number is sufficiently small. Table 4 shows K_0 computed in the resolved PM and underresolved PM cases. In contrast to the case in Section 4.5, the underresolved PM case with the solid assignment outputs comparable K_0 to one in the resolved PM case. This is because the main flow passages through the domain exist and largely contribute to K_0 . Qualitatively, due to less connectivity of large-scale PM, K_0 is slightly reduced from the resolved PM case. On the other hand, the PM model enhanced their connectivity and resulted in a slightly higher K_0 . All three cases show almost comparable K_0 within the 6% deviation and consistent velocity profiles in Fig. 16. This fact demonstrates that the PM model works properly, reproducing the proper high resistivity in the PM regions. Moreover, the computational cost for simulation is saved from the resolved PM case to the underresolved PM case with the PM model by a factor of 5.

In the simulation for computing P_C , the domain settings, initial conditions, wettability condition, and simulation processes follow the same manner as the P_C simulation in Fig. 4. Viscosities for both components are set as $\nu_w = \nu_o = 1.66 \times 10^{-3}$. The simulated capillary pressure, ΔP , in terms of the water saturation S_w is shown in the top figure of Fig. 17. Here, a resolution factor of 5 is multiplied by ΔP for the resolved PM case for fair comparisons in the lattice unit. According to the displayed S_w in the underresolved PM case with the solid assignment, the volume of the underresolved PM, which is regarded as solid in this case, is assumed to be filled by 89 % water all time. The water distributions at certain stages, marked with the dotted circles in the top figure, are shown in the bottom figures using the light-blue isosurfaces of $At > 0.5$ and color contours on the central cutting plane. Between $\Delta P \approx 0.04$ and $\Delta P \approx 0.02$, the water mainly invades the small-scale PM regions. Without the PM model, this stage cannot be simulated. The underresolved PM case with the PM model shows reasonably consistent results with the resolved PM case. Between $\Delta P \approx 0.02$ and $\Delta P \approx 0.0$, the water mainly invades the large-scale PM regions. As seen in the P_c curve, all three cases show excellent agreements at this stage. Between $\Delta P \approx 0.0$ and $\Delta P \approx -0.055$, the oil in the remaining spaces is washed out. At this stage, connectivity among large-scale PM regions plays an important role.

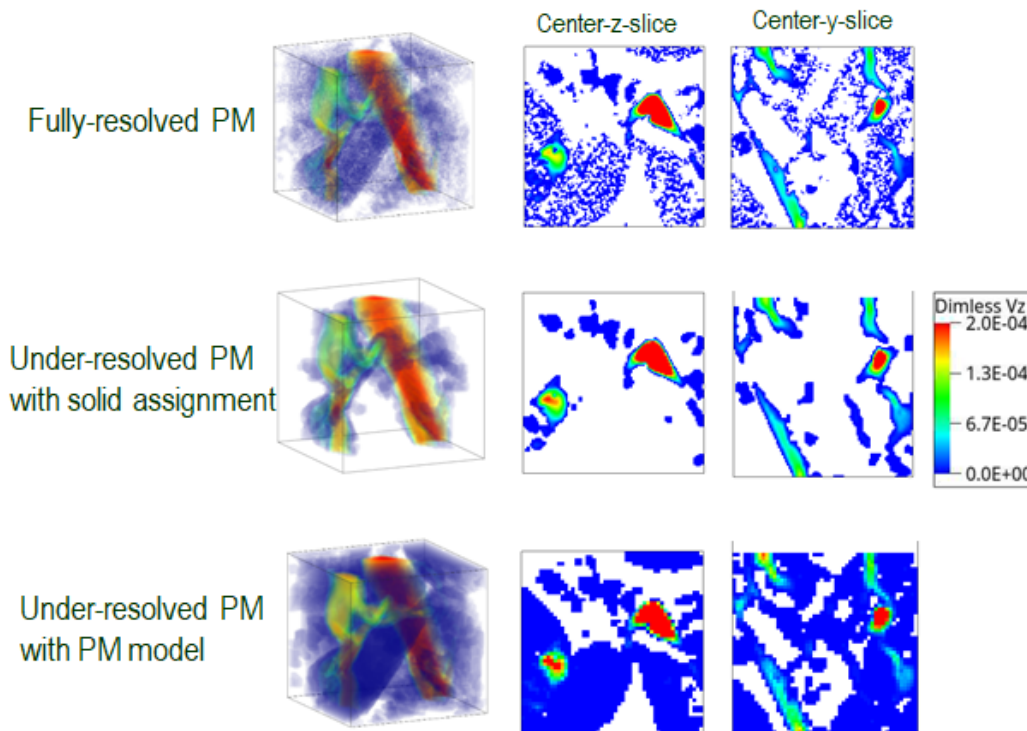


Figure 16: Dimensionless velocity profiles over the domain (left column) and on the center z- (center column) and y- (right column) slices. Velocity is nondimensionalized by gL^2/ν . The resolved PM case (top row), the under resolved PM case with the solid assignment (middle row), and the underresolved PM case with the PM model (bottom row) are compared.

At the last stage of the imbibition process, the residual component patterns are shown in Fig. 18 with an isosurface of $At < -0.5$. Although it is difficult to compare their detailed structures by looking at the isosurfaces at different resolutions, it may be fair to compare the distribution of major blobs. Indeed, we observe that the underresolved PM case without the PM model misses some of the large oil blobs in the resolved PM case, but the PM model successfully captures them consistently. Moreover, the computational cost in the underresolved PM case is saved by a factor of 43 compared to the resolved PM case.

4.7 Relative permeability with coarsened images of sampled porous media

In the simulation computing the relative permeability K_r in Fig. 4, the sampled PM in Fig. 3 is fully resolved with a resolution of $0.758 \mu\text{m}/\text{pixel}$. In this section, the images are coarsened by 16 times, and then the size of the computational domain becomes $16 \times 16 \times 16$, in which the PM structure is underresolved everywhere and has to be treated by the PM model. In this section, we check if the PM model can reproduce the comparable K_r with the fully resolved PM case. The domain, gravity, and wettability are set in the

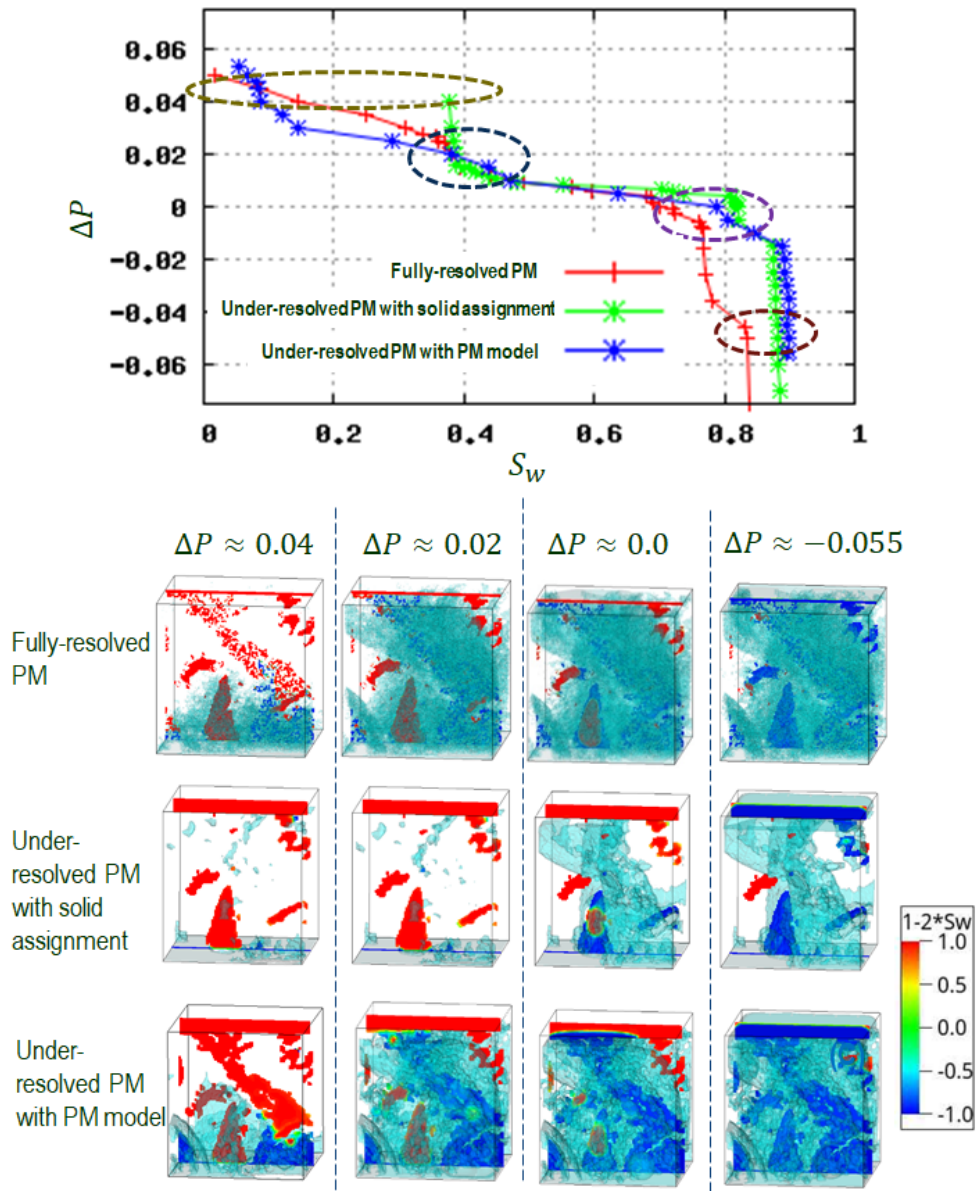


Figure 17: Capillary pressure curve in terms of water saturation S_w in the resolved PM case and the underresolved PM case with the solid assignment and with the PM model in the top figure. In the bottom figures, the water distributions at certain stages, marked with the dotted circles in the top figure, are shown for all cases using the isosurface of $At > 0.5$ and color contour of At on the central cutting plane.

same manner as the K_r simulation in Fig. 4. The viscosity for both components is set as 3.33×10^{-3} .

In Fig. 19, the resulting K_r curves are compared with the input K_r curves, which are from the fully resolved case in Fig. 4. They show excellent agreement. Additionally, in the

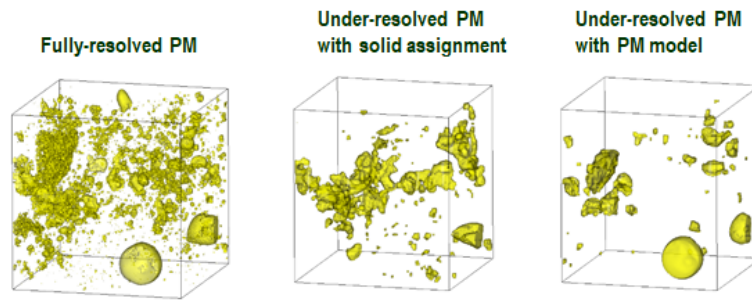


Figure 18: Residual oil patterns at the last stage of the imbibition process, $\Delta P \approx -0.055$ displayed by the isosurface of $At < -0.5$.

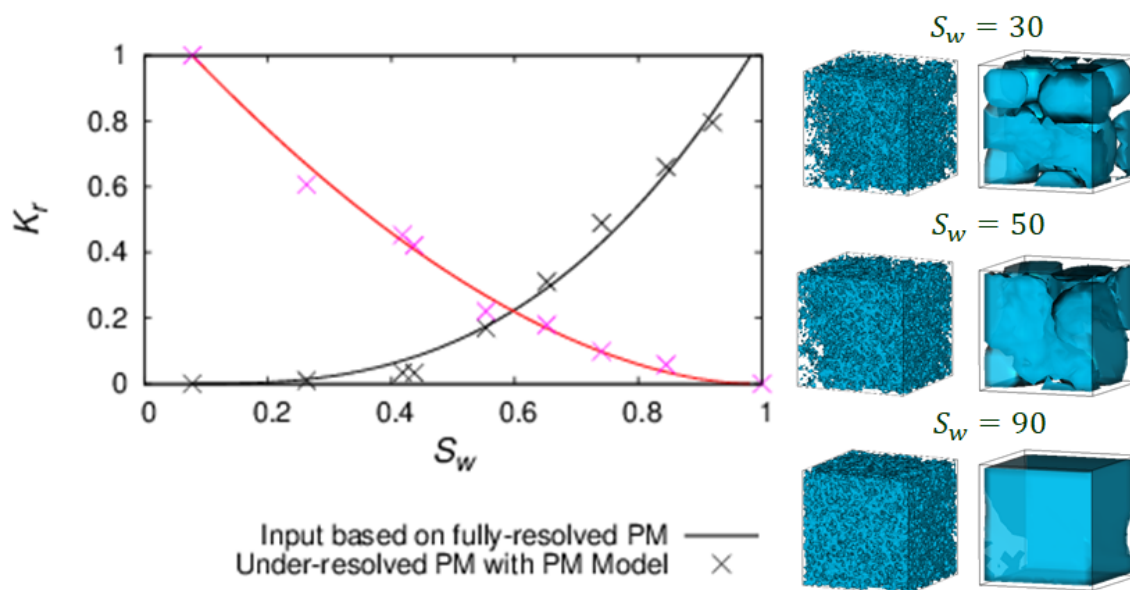


Figure 19: Relative permeability in the underresolved PM case with black crosses for K_{rw} and purple crosses for K_{ro} . The red and black lines are the input K_r based on the fully resolved PM case in Fig. 4. On the right, the water distribution is compared between the fully resolved PM (left) and underresolved PM (right) cases at certain options of S_w .

right images, the water distributions are compared at certain options of S_w between the fully resolved PM case and the underresolved PM case. Although it is difficult to compare detailed water distributions under such a large resolution difference, we try to show them using the isosurface of $S_w \cdot \phi > 0.9$ for the fully resolved PM case and $S_w \cdot \phi > 0.35$ for the underresolved PM case. The results show that the water volume grows homogeneously in both cases. As a result, the proposed multiscale approach allows us to perform a consistent K_r simulation in the underresolved PM with the fully resolved PM case. Due to the coarsened resolution, the simulation time is saved by 200 times from the fully resolved PM case.

5 Summary

Computational models and a workflow for efficient two-component flow simulations in multiscale solid structures are proposed and validated through a set of benchmark test cases. Specifically, using precomputed physical properties such as the absolute permeability K_0 , capillary pressure P_C , and relative permeability K_r for representative porous structures, together with the local PM and fluid information such as the porosity and water saturation, local fluid force is constructed in the multiscale simulation to account for viscous, capillary, and pressure effects in underresolved porous media (PM) regions. In this way, flow simulation in multiscale solid structures becomes feasible with practical resolution. The validation is conducted by comparing with analytic solutions and computed results with much finer-resolution corresponding cases resolving the PM structures fully. In addition to artificially established systems, the tested benchmarks include in-house designed geometries for multiscale complex porous structures.

In the K_0 simulation, compared with analytic solutions, it is confirmed that the PM model works accurately for viscous force as expected. This result shows consistency with the Darcy solver within 1% accuracy in the multitype PM case. Additionally, compared with the resolved PM case, K_0 in the underresolved PM case with the PM model is consistent within 6% accuracy in the in-house designed PM case. The simulation cost is reduced by a factor of 20 at best. In the P_C simulation, compared with the analytic solution, it is confirmed that the PM model can accurately reproduce the capillary force and can also quantitatively reproduce the typical sequential imbibition process in PM and pores. Moreover, in the in-house designed PM case, the entry pressures to both PM and pores agree well between the underresolved PM case with the PM model and the resolved PM case. The PM model successfully captures the major residual oil blobs at the last stage of the imbibition process, consistent with the resolved PM case. The simulation cost is reduced by a factor of 43 at best. In the K_r simulation, comparing the fully resolved PM case, the PM model can accurately reduce the relative permeability and water distributions in the underresolved PM using the PM model. The simulation cost is saved by a factor of 200 at best.

Further applications of this underresolved simulation approach for reservoir rock can be found in [38]. The models and methodology in this study can be extensively applied to various engineering systems of multiscale porous structures, such as the example cases in the introduction. Accordingly, further explorations and developments are expected in the near future.

References

- [1] H. Otomo, R. Salazar-Tio, H. Chen, R. Zhang, A. Fager, G. Blasubramanian, B. Crouse, H. Fan and J. Yang, Computer simulation of multi-phase and multi-component fluid flows including physics of under-resolved porous structures, US Patent No. 17136259, (2020).

- [2] Y. Han and K. Liu, Integrated digital rock construction workflow for chemical enhanced oil recovery numerical simulation, *Energy Fuels*, 35 (2021), 14734-14745.
- [3] A. Shirbazo, A. Taghavinejad and S. Bagheri, CO₂ capture and storage performance simulation in depleted shale gas reservoirs as sustainable carbon resources, *Journal of Construction Materials* (2021).
- [4] P. Xu, S. Qiu, J. Cai, C. Li and H. Liu, A novel analytical solution for gas diffusion in multi-scale fuel cell porous media, *J. Power Sources*, 362 (2017), 73-79.
- [5] B. Xiao, W. Wang, X. Zhang, G. Long, H. Chen, H. Cai and L. Deng, A novel fractal model for relative permeability of gas diffusion layer in proton exchange membrane fuel cell with capillary pressure effect, *Fractals*, 27 (2019), 1950012.
- [6] M. Mortazavi, A. D. Santamaria, V. Chauhan, J. Z. Benner, M. Heidari and E. F. Médici, Effect of PEM fuel cell porous media compression on in-plane transport phenomena, *J. Power Sources Adv.*, 1 (2020), 100001.
- [7] E. Cariaga, F. Concha and M. Sepúlveda, Flow through porous media with applications to heap leaching of copper ores, *Chem. Eng. J.*, 111 (2005), 151-165.
- [8] A. Tcharkhtchi, N. Abbasnezhad, M. Z. Seydani, N. Zirak, S. Farzaneh and M. Shirinbayan, An overview of filtration efficiency through the masks: Mechanisms of the aerosols penetration, *Bioact. Mater.*, 6 (2021), 106-122.
- [9] T. Bultreys. Savonnières carbonate. Digital Rocks Portal <http://www.digitalrockportal.org/projects/72>, (2016).
- [10] D. M. Freed, Lattice-Boltzmann method for macroscopic porous media modelling, *Int. J. Mod. Phys. C*, 09 (1998), 1491-1503.
- [11] N. S. Martys and J. G. Hagedorn, Multiscale modeling of fluid transport in heterogeneous materials using discrete Boltzmann methods, *Mater. Struct.*, 35 (2002), 650-658.
- [12] I. Ginzburg, G. Silva and L. Talon, Analysis and improvement of Brinkman lattice Boltzmann schemes: bulk, boundary, interface. Similarity and distinctness with finite elements in heterogeneous porous media, *Phys. Rev. E*, 91 (2015), 023307.
- [13] J. Li and D. Brown, Upscaled lattice Boltzmann method for simulations of flows in heterogeneous porous media, *Geofluids*, 1740693 (2017).
- [14] J. Zhu and J. Ma, Extending a gray lattice Boltzmann model for simulating fluid flow in multi-scale porous media, *Sci. Rep.*, 8 (2018), 1-19.
- [15] A. Fager, G. Balasubramanian, B. Crouse and D. Freed, Prediction of shale matrix permeability controls through simulation of advection and diffusion processes, RMAG/DWLS Fall Symposium, Denver (2019).
- [16] M. Zhang, R. Salazar-Tio, A. Fager and B. Crouse, A multiscale digital rock workflow for shale matrix permeability prediction, Unconventional Resources Technology Conference URTEC, (2020), 2416-2432.
- [17] O. Dinariev, N. Evseev and D. Klemin, Density functional hydrodynamics in multiscale pore systems: Chemical potential drive, The 2019 International Symposium of the Society of Core Analysts, 01001 (2020), 1-10.
- [18] M. Suhrer, X. Nie, J. Toelke and S. Ma, Upscaling method for obtaining primary drainage capillary pressure and resistivity index with digital rock physics, International Petroleum Technology Conference, 20035 (2020).
- [19] Q. Li, K. H. Luo and X. J. Li, Forcing scheme in pseudopotential lattice Boltzmann model for multiphase flows, *Phys. Rev. E*, 86 (2012), 016709.
- [20] X. Shan and H. Chen, Lattice Boltzmann model for simulating flows with multiple phases and components, *Phys. Rev. E*, 47 (1993), 1815.

- [21] X. Shan and H. Chen, Simulation of nonideal gases and liquid-gas phase transitions by the lattice Boltzmann equation, *Phys. Rev. E*, 49 (1994), 2941.
- [22] H. Chen, R. Zhang, I. Staroselsky and M. Jhon, Recovery of full rotational invariance in lattice Boltzmann formulations for high Knudsen number flows, *Physica A*, 362 (2006), 125-131.
- [23] R. Zhang, X. Shan and H. Chen, Efficient kinetic method for fluid simulation beyond the Navier-Stokes equation, *Phys. Rev. E*, 74 (2006), 046703.
- [24] J. Latt and B. Chopard, Lattice Boltzmann method with regularized pre-collision distribution functions, *Math. Comput. Simulat.*, 72 (2006), 165-168.
- [25] X. Shan, X. Yuan and H. Chen, Kinetic theory representation of hydrodynamics: A way beyond the Navier-Stokes equation, *J. Fluid. Mech.*, 550 (2006), 413-441.
- [26] Y. Qian, D. d'Humières and P. Lallemand, Lattice BGK models for Navier-Stokes equation, *Europhys. Lett.*, 17 (1992), 479.
- [27] H. Chen, C. Teixeira and K. Molving, Digital physics approach to computational fluid dynamics: some basic theoretical features, *Int. J. Mod. Phys. C*, 8 (1997), 675-684.
- [28] H. Chen, R. Zhang and P. Gopalakrishnan, Lattice Boltzmann collision operators enforcing isotropy and Galilean invariance, *US Patent No. 9,576,087*, (2017).
- [29] H. Chen, R. Zhang and P. Gopalakrishnan, Filtered lattice Boltzmann collision formulation enforcing isotropy and Galilean invariance, *Phys. Scr.*, 95 (2020), 034003.
- [30] H. Chen, C. Teixeira and K. Molving, Realization of fluid boundary conditions via discrete Boltzmann dynamics, *Int. J. Mod. Phys. C*, 9 (1998), 1281-1292.
- [31] Y. Li, R. Zhang, R. Shock and H. Chen, Prediction of vortex shedding from a circular cylinder using a volumetric Lattice-Boltzmann boundary approach, *Eur. Phys. J. Special Topics*, 171 (2009), 91-97.
- [32] Y. Li, R. Shock, R. Zhang and H. Chen, Numerical study of flow past an impulsively started cylinder by the lattice-Boltzmann method, *J. Fluid. Mech.*, 519 (2004), 273-300.
- [33] H. Fan, R. Zhang and H. Chen, Extended volumetric scheme for lattice Boltzmann models, *Phys. Rev. E*, 73 (2006), 066708.
- [34] H. Otomo, H. Fan, R. Hazlett, Y. Li, I. Staroselsky, R. Zhang and H. Chen, Simulation of residual oil displacement in a sinusoidal channel with the lattice Boltzmann method, *C. R. Mecanique*, 343 10 (2015), 559-570.
- [35] H. Otomo, H. Fan, Y. Li, M. Dressler, I. Staroselsky, R. Zhang and H. Chen, Studies of accurate multi-component lattice Boltzmann models on benchmark cases required for engineering applications, *J. Comput. Sci.*, 17 (2016), 334-339.
- [36] H. Otomo, B. Crouse, M. Dressler, D. M. Freed, I. Staroselsky, R. Zhang, H. Chen, Multi-component lattice Boltzmann models for accurate simulation of flows with wide viscosity variation, *Comput. Fluids*, 172 (2018) 674-682.
- [37] L. F. Konikow and J. D. Bredehoeft, Computer model of two-dimensional solute transport and dispersion in ground water, *US Government Printing Office*, 7 (1978).
- [38] A. Fager, R. Salazar-Tio, H. Otomo, G. Balasubramanian, B. Crouse, and J. Schembre-McCabe, SCA2021-U004 (accepted).
- [39] B. Crouse, X. Nie, R. Zhang, Y. Li, H. Otomo, H. Chen and A. Fager, Mass exchange model for relative permeability simulation, *US 16/511 221*, (2019).